


Magnetic ground states of a model for $M\text{Nb}_3\text{S}_6$ ($M = \text{Co}, \text{Fe}, \text{Ni}$)O. Heinonen^{1,*}, R. A. Heinonen², and H. Park^{1,3}¹Materials Science Division, Argonne National Laboratory, Lemont, Illinois 60439, USA²Department of Physics and INFN, University of Rome “Tor Vergata,” Via della Ricerca Scientifica 1, 00133 Rome, Italy³Department of Physics, University of Illinois, Chicago, Illinois 60607, USA (Received 28 September 2021; revised 22 December 2021; accepted 25 January 2022; published 14 February 2022)

The transition-metal-intercalated dichalcogenide CoNb_3S_6 is a triangular antiferromagnet (AFM) that has recently been shown to exhibit a large anomalous Hall effect (AHE) below the Néel temperature, even though the response to an external field is very small. This suggests that there is an interesting magnetic structure that interacts with the electronic structure to yield the AHE, as collinear AFMs cannot exhibit a nonzero AHE. We propose a model for magnetic transition-metal-intercalated dichalcogenides and examine its ground state as a function of interaction parameters. The model exhibits transitions between planar spin spirals, nonplanar spin spirals, and a particular noncoplanar so-called $3q$ state. This latter state must exhibit a nonzero AHE, while the spin spirals do not.

DOI: [10.1103/PhysRevMaterials.6.024405](https://doi.org/10.1103/PhysRevMaterials.6.024405)

I. INTRODUCTION

Ferromagnetic (FM) and antiferromagnetic (AFM) systems can be frustrated when all interactions cannot be simultaneously minimized. For FMs, frustration involves more than near-neighbor interactions. The frustration can in FMs lead to several ordered states with complex orders, such as spiral states and skyrmion crystals [1–4]. In contrast, AFMs are in a sense easier to frustrate because, in certain lattices, frustration is a geometrical property, and near-neighbor interactions alone will lead to frustration and complex orders [5]. Classic examples of a frustrated AFM are the triangular Ising AFM, the ground state of which was solved in two dimensions (2D) by Wannier [6,7], or the 2D triangular XY and Heisenberg AFMs with Néel ground states in which the three spins on an elementary triangular plaquette are 120° degrees apart. More generally, triangular AFMs can also exhibit a number of different collinear and noncollinear states [8]. Another class of frustrated AFMs are the kagome AFMs [9–12], such as Mn_3Ge . AFMs have recently become the focus of intense interest in connection with topological materials and their magnetotransport properties. There exist quite a few examples of materials that are kagome AFMs or ferrimagnets with linked magnetic and topological properties, for example, Mn_3Ge and Mn_3Sn [13–20] as well as others, such as $(RE)\text{Mn}_6\text{Sn}_6$, with $RE = \text{rare earth}$ [21–24], and MnBi_2Te_4 [25–29]. In addition to nearest-neighbor interactions that are ubiquitous in AFMs, if the crystal is not centrosymmetric, a chiral Dzyaloshinskii-Moriya interaction (DMI) is allowed. The direction of the DMI vector \mathbf{d}_{ij} that couples spins at sites i and j in the same plane depends on the in-plane symmetry. For example, in kagome AFMs, the DMI vector is along the crystallographic c axis, perpendicular to the kagome plane.

A phenomenon that connects magnetotransport to the topology of the electronic structure is the anomalous Hall effect (AHE). Modern theories directly relate the AHE to the Berry phase of the electronic bands in the first Brillouin zone (BZ) [2,30–34]. There are also direct connections between the real-space magnetic structure of AFMs and the AHE [35–37]. A real-space magnetic texture with a finite chirality can give rise to a fictitious magnetic field that, in turn, produces a Hall effect [38–40]. The chirality is defined as $\chi = \epsilon_{123}\mathbf{S}_1 \cdot (\mathbf{S}_2 \cdot \mathbf{S}_3)$, where \mathbf{S}_i , $i = 1, 2, 3$ are three spins on an elementary triangular plaquette for the case of triangular or kagome systems, and ϵ_{ijk} is the Levi-Civita symbol. This is the same concept that, in the continuum limit, gives rise to a topological magnetic field and a topological Hall effect in magnetic skyrmions [41]. In the presence of spin-orbit coupling, the relation between real-space spin texture and Berry curvature becomes complicated. For example, gapless collinear AFMs cannot exhibit an AHE [42–44]. Coplanar kagome or triangular AFMs such as Mn_3Ge or PdCrO_2 can exhibit an AHE [13,14,45] only in the presence of spin-orbit coupling or a small net moment that breaks certain symmetries [13], while noncoplanar AFMs with nonzero chirality can exhibit a nonzero AHE [35–37]. In general, if the system is invariant under the combination of time reversal \mathcal{T} and a lattice translation \mathcal{R} , the Berry phase is zero, and the chirality is also zero. More generally, if the system is invariant under the combination of \mathcal{T} and \mathcal{O} , where \mathcal{O} is any unitary symmetry operator, the Berry phase is zero. Conversely, if the system is not invariant under \mathcal{TR} , the Berry phase and the chirality can both be nonzero. Therefore, a nonzero chirality for a noncoplanar system is an indication that there can be a nonzero Berry phase and a nonzero AHE.

A family of triangular magnets are the intercalated $(M)\text{Nb}_3\text{S}_6$ compounds, where M is Ni, Co, Fe, or Mn. These materials are dichalcogenides [46] $(M)_x\text{NbS}_2$ in which M are intercalated between prismatic layers of NbS_2 and are stable

*heinonen@anl.gov

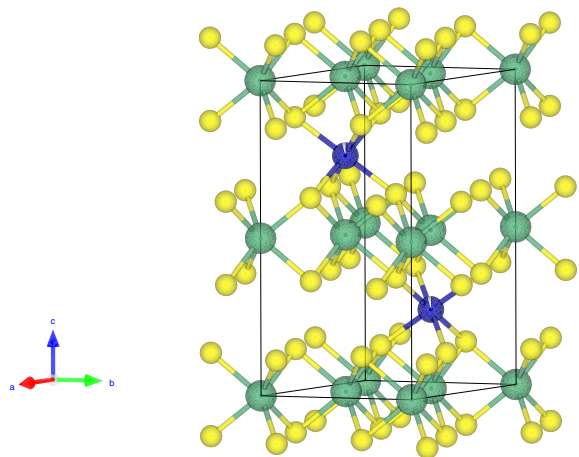


FIG. 1. Unit cell of CoNb_3S_6 with Co in blue, Nb in green, and S in yellow, with the directions of lattice vectors a (red), b (green), and c (blue) indicated.

and ordered at $x = \frac{1}{3}$. The unit cell for CoNb_3S_6 is depicted in Fig. 1. The crystal structure and magnetic susceptibilities were first investigated by Anzenhofer *et al.* [46], who also discussed their electronic structure. Parkin *et al.* [47] used neutron diffraction on single-crystal samples of CoNb_3S_6 and CoTa_3S_6 to determine the AFM magnetic structure of these two compounds. They concluded that the magnetic structure is orthohexagonal with two Co atoms per magnetic unit cell, with a moment of $2.73 \mu_B$ for Co, slightly lower than the spin-only moment of $3 \mu_B$ for Co^{2+} . More recently, Ghimire *et al.* [44] performed magnetic measurements and magnetotransport measurements on CoNb_3S_6 . They found a small linear susceptibility for in-plane and out-of-plane (OOP) magnetic fields ($< 0.1 \mu_B$ per formula unit for a field of 6 T), with the OOP susceptibility larger than the in-plane one, but with a pronounced hysteresis in the OOP susceptibility at temperatures < 29 K. Magnetotransport measurements yielded a relatively large AHE below the Néel temperature T_N , which is 27.5 K. They argued that a magnetic-field-induced component OOP was not large enough to give rise to the observed AHE. Based on electronic structure calculations, they suggested that CoNb_3S_6 is a magnetic Weyl semimetal with a complex noncollinear magnetic structure. Later, Tenasini *et al.* [48] performed further magnetotransport experiments and found an AHE per Co layer close to the quantized value of e^2/h , suggesting that the Co layers form topologically nontrivial 2D bands.

The precise magnetic structure of $(M)\text{Nb}_3\text{S}_6$ remains elusive, but the works by Ghimire *et al.* [44] and Tenasini *et al.* [48] suggest that there is a connection between the magnetic and electronic structures, giving rise to nontrivial topology and a large AHE. In this paper, we look for magnetic order as a possible source for a nonzero AHE. We propose magnetic ground states for a model of the $(M)\text{Nb}_3\text{S}_6$ systems. We find that, depending on the ratio of coupling constants, the ground state can be either a noncollinear, noncoplanar AFM with nonzero chirality, or spiral states $1q$ and $2q$ defined, respectively, by a single wave vector \mathbf{q} or by two wave

vectors \mathbf{q} and \mathbf{q}_2 in the first BZ, and particularly \mathbf{q}_2 is incommensurate with the in-plane lattice constant. In addition, the spiral states have zero chirality: the $1q$ state is invariant under the combination of \mathcal{T} and \mathcal{R} . This makes the contribution to the AHE from a real-space chirality and the Berry phase vanish, and the $1q$ magnetic state in $(M)\text{Nb}_3\text{S}_6$ cannot yield a nonzero AHE [13,45]. The $2q$ state is more complicated: it is in general noncoplanar and has a local chirality that does not vanish, but the average chirality over many plaquettes vanishes, which implies that the AHE will, too. This means that the AHE can be a discriminant of the magnetic ground states. The ground state we find for a range of interaction parameters is consistent with the ground state obtained from electronic structure calculations including spin-orbit interactions [49]. This paper is organized as follows. In Sec. II, we introduce the magnetic Hamiltonian, and in Sec. III, we discuss finite-temperature atomistic simulations and introduce general variational ground states for the different candidate states. We present our results in Sec. III, and Sec. IV contains conclusions and a summary.

II. METHODS

A. Model Hamiltonian

Experimental evidence makes clear that $(M)\text{Nb}_3\text{S}_6$ undergo magnetic transitions from paramagnetic to ordered magnetic states [44,46–48] at temperatures of ~ 30 K or higher. First-principles calculations [49] yield M moments ranging from $1.4 \mu_B$ ($M = \text{Ni}$) to $4.9 \mu_B$ ($M = \text{Mn}$), and experimental measurements [47] also indicate a large Co moment of $2.73 \mu_B$. These are temperature ranges and magnetic moments for which classical spin models are usually applied successfully. We are furthermore not aware of any evidence that quantum spin fluctuations play an important role in the magnetic structure or transport measurements. We will therefore use classical spin models to describe these systems. We assume that the magnetization can be described by local moments on the M atoms and start with a minimal classical Heisenberg model with near-neighbor in-plane AFM coupling J , biquadratic coupling B , and near-neighbor OOP coupling J_3 (see Fig. 2). The moments are located on a triangular lattice in the crystallographic ab plane, which we will take to be the xy plane, with lattice constant a , and we take the z axis to be along the crystallographic c axis, so the sites of the Co atoms are given by

$$\mathbf{r}_i = m_i \left(\frac{\sqrt{3}}{2} a \hat{x} + \frac{a}{2} \hat{y} \right) + n_i a \hat{y} + \ell c \hat{z} + \text{Mod}(\ell, 2) \frac{\sqrt{3}}{4} a \hat{x}, \quad (1)$$

where m_i , n_i , and ℓ are integers. Because inversion symmetry is broken, a DMI is allowed, with the general form:

$$H_{\text{DMI}} = \sum_{\langle i, j \rangle} \mathbf{d}_{ij} \cdot [\mathbf{S}(\mathbf{r}_i) \cdot \mathbf{S}(\mathbf{r}_j)], \quad (2)$$

where the sum $\langle i, j \rangle$ is over in-plane nearest neighbors on sites \mathbf{r}_i and \mathbf{r}_j . Based on symmetry, the DMI vector must be directed along the crystallographic c axis. There are then two possible ways to arrange the DMI vectors: along the $+z$ axis or along the $-z$ axis. We do not know if the DMI vectors point up or down, but for the purposes of our work here, which one

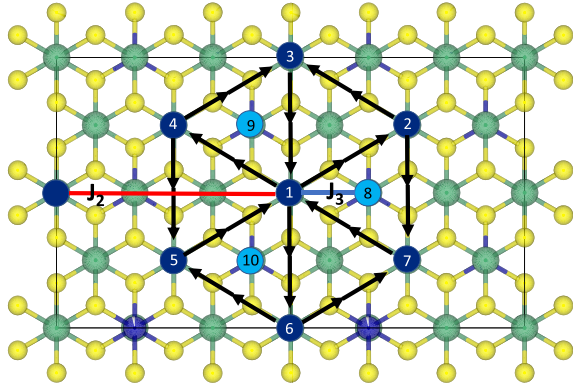


FIG. 2. View of CoNb_3S_6 in the ab plane. Co atoms in dark blue are on one lattice plane along the c axis and light blue ones on neighboring planes. In the plane, the Co atom labeled 1 interacts with the in-plane nearest neighbors 2–7, with in-plane next-nearest neighbors as indicated by the red line, and with out-of-plane neighbors at the sites 8–10 as indicated by a blue line. The arrows on the bonds indicate the order of the cross product for the near-neighbor Dzyaloshinskii-Moriya interaction (DMI).

is lower in energy is immaterial, and we will take the DMI vectors to point up. We will also assume that there is a single-site anisotropy with the ab plane an easy plane, consistent with the experimentally observed larger OOP susceptibility than the in-plane one [44]. The three-dimensional (3D) classical Hamiltonian is then

$$\mathcal{H}_{3\text{D}} = H_{\text{exchange}} + H_{\text{nn ex}} + H_{\text{OOP}} + H_{\text{DMI}} + H_{\text{biq}} + H_{\text{ani}} + H_{\text{Z}}. \quad (3)$$

The nearest-neighbor in-plane exchange interaction is

$$H_{\text{exchange}} = \frac{J}{2} \sum_{\langle i,j \rangle} \mathbf{S}(\mathbf{r}_i) \cdot \mathbf{S}(\mathbf{r}_j), \quad (4)$$

where we will take J to be unity and to be the energy scale. We include an in-plane next-nearest neighbor exchange:

$$H_{\text{nn ex}} = \frac{J_2}{2} \sum_{\langle\langle i,j \rangle\rangle} \mathbf{S}(\mathbf{r}_i) \cdot \mathbf{S}(\mathbf{r}_j), \quad (5)$$

where the notation $\langle\langle i,j \rangle\rangle$ means that i and j are in-plane next-nearest neighbors. The near-neighbor OOP exchange is

$$H_{\text{OOP}} = \sum_{\langle i,j \rangle, \text{OOP}} \frac{J_3}{2} \mathbf{S}(\mathbf{r}_i) \cdot \mathbf{S}(\mathbf{r}_j), \quad (6)$$

with the sum over OOP near-neighbor sites i and j . We will assume that $J_3 < J$. This is not unreasonable, as the OOP bond length is larger than the in-plane one by ~ 1 Å. This is in any case not important as J_3 just sets a scale for the interplane order which, as we show below [Eqs. (11) and (12)], is commensurate with the lattice spacing c .

The DMI is

$$H_{\text{DMI}} = \sum_{\langle i,j \rangle} D \mathbf{d} \cdot [\mathbf{S}(\mathbf{r}_i) \times \mathbf{S}(\mathbf{r}_j)], \quad (7)$$

where D is the coupling strength and $\mathbf{d} = \hat{\mathbf{z}}$ is the DMI vector. The biquadratic exchange and uniaxial anisotropy are, respectively,

$$H_{\text{biq}} = \frac{B}{2} \sum_{\langle i,j \rangle} [\mathbf{S}(\mathbf{r}_i) \cdot \mathbf{S}(\mathbf{r}_j)]^2, \quad (8)$$

and

$$H_{\text{ani}} = K \sum_i (S_{z,i})^2, \quad (9)$$

with B and K the respective coupling strengths and $K > 0$ for the ab plane an easy plane. In addition, in the presence of an external field \mathbf{H}_{ext} , there is a Zeeman energy:

$$H_{\text{Z}} = - \sum_i \mathbf{H}_{\text{ext}} \cdot \mathbf{S}(\mathbf{r}_i). \quad (10)$$

Figure 2 depicts a view of CoNb_3S_6 in the ab plane. Co atoms in one plane along the c axis are indicated in dark blue. The Co at site 1 interacts with its nearest neighbors on sites 2 to 7 via the Heisenberg interaction and the DMI; the order for the cross product in the DMI in elementary triangular plaquettes is indicated with the black arrows. The Co at site 1 also interacts with its in-plane next-nearest neighbor through a coupling J_2 , as indicated by the red line. The sites colored light blue and labeled 8 to 10 are Co atoms in the plane above or below site 1, and the Co atom at site 1 interacts with these six sites through a coupling J_3 indicated with a blue line.

It is not impossible that there are longer-range interactions in these compounds. For example, because $(M)\text{Nb}_3\text{S}_6$ are metallic, there may be long-range Ruderman-Kittel-Kasuya-Yosida (RKKY) interactions mediated by electrons at the Fermi surface, and such interactions could lead to longer-range order such as spiral structures along the c axis. However, because of the intercalated nature of these compounds with a large distance between consecutive M planes, the OOP resistivity (along the c axis) is more than an order of magnitude larger than the in-plane resistivity [48]. This makes RKKY interactions along the c axis unlikely to be large enough to have a significant effect. One may of course include more in-plane couplings. However, our model already includes four in-plane couplings that extend up to 10 Å through the next-nearest neighbor interactions. We are also interested in a minimal model that can explain the magnetic structures and the appearance of a large AHE in CoNb_3S_6 , and we believe our model can. We will therefore not try to extend it to include more interactions (which would also necessarily make analyses more complicated).

Given the Hamiltonian $\mathcal{H}_{3\text{D}}$ in Eq. (3), there are a few properties of the magnetic order one may expect. Because the system is a triangular AFM with ABAB stacking, the system should have a simple commensurate order along the c axis [50]. A simple argument illustrates this: Given the structure of the Hamiltonian Eq. (3) with decoupled in-plane and OOP couplings, one can assume that the spin configuration in an ordered state is separable into in-plane and OOP components,

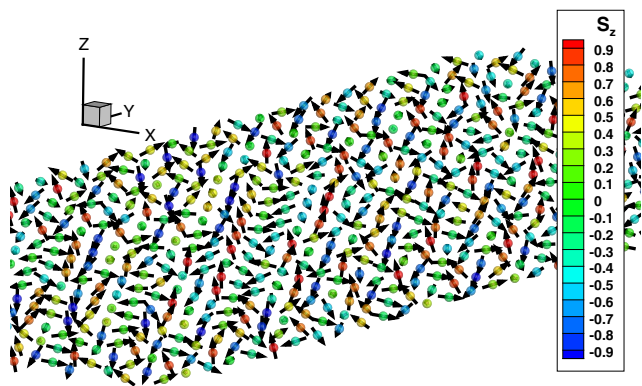


FIG. 3. Snapshot of the spin configuration in a M plane for $B = 0.4$, $K = 0.1$, $D = 0$, $J_2 = 0.08$, $J_3 = 0.2$, and $k_B T \approx 0.01$. The arrows show the three-dimensional (3D) spin orientation, and the color coding denotes the z component of the spins. The snapshot shows there is short-range local order in small domains.

and the latter can be Fourier transformed:

$$\mathbf{S}(\mathbf{r}_i) = \frac{1}{N_z} \sum_{q_z} \mathbf{S}(x_i, y_i, q_z) e^{iq_z z_i}, \quad (11)$$

where N_z is the number of M planes. This immediately leads to an effective OOP coupling by summing over the six OOP near neighbors that couple to the spin at site \mathbf{r}_i :

$$H_{\text{OOP}} = \frac{J_3}{N_z} \sum_{q_z, (i,j), \text{OOP}} \cos(q_z c) \mathbf{S}(x_i, y_i, q_z) \mathbf{S}^*(x_j, y_j, q_z), \quad (12)$$

which is minimized for $q_z = 0$ ($J_3 < 0$, FM OOP coupling) or $q_z = \pi/c$ ($J_3 > 0$, AFM OOP coupling), as the in-plane couplings J , J_2 , and B are all AFM, and as we shall argue later at the end of Sec. III A, D must be small. This means that we can expect the order along the c axis to be trivial, irrespective of the sign of J_3 . Furthermore, given the nature of the DMI, we expect that increasing the DMI will tend to make the in-plane spin order coplanar, at least for spin spiral state, to minimize the DMI energy. Finally, the next-nearest neighbor interaction can lead to an instability of the in-plane static susceptibility at the M points in the BZ [36,40], which can

potentially lead to the emergence of a $3q$ state. The $3q$ state is a noncoplanar AFM with a nonzero chirality; such a state can give rise to a nonzero AHE because the nonzero chirality corresponds to a Berry phase [36].

To establish some basic features of the low-temperature magnetic structure of \mathcal{H}_{3D} in Eq. (3), particularly to confirm the trivial OOP order, we performed Monte Carlo simulations and also simulations integrating the stochastic Landau-Lifshitz-Gilbert (s-LLG) equation [51] based on the Hamiltonian \mathcal{H}_{3D} at fixed temperature using the VAMPIRE software [52]. For the fixed-temperature s-LLG simulations, we used a time step of 0.1 fs and a dimensionless damping $\alpha = 0.1$, thermally randomized the spins at a high temperature $k_B T \approx 1$ for 1 ns (10^5 time steps), and then quenched the system to a low temperature $k_B T \approx 0.01$. We used an orthorhombic supercell with dimensions $9.99047 \times 23.0720 \times 11.886$ nm containing 16 000 atoms. As one might expect, short-range in-plane order emerged at low temperatures $T \sim J$ and long-range order at a temperature set by J_3 . A main conclusion of these 3D simulations was that the order along the c axis was always trivial, as the arguments above suggest, whether J_3 was FM ($J_3 < 0$) or AFM ($J_3 > 0$) with consecutive planes along c having the same in-plane order shifted by an in-plane translation: The OOP coupling leads to a trivial order along the c axis, without any effect on the in-plane order. Figure 3 shows a snapshot of the spin configuration in an ab plane for $B = 0.4$, $J_2 = 0.08$, $D = 0$, $J_3 = 0.2$, and $k_B T \approx 0.01$. There appears to be some local order, but there are multiple domains in the imaged region. It should be noted that, at this low temperature, only very small thermal noise can be discerned as a function of time. The difficulty in identifying the nature of the order is often the case for finite-sized simulations when the order may be incommensurate with the lattice spacing. Figure 4 shows snapshots of the spin configurations for the same parameters B , D , and J_3 but now with $J_2 = 0.3$ (left panel) and $J_2 = 0.5$ (right panel). In these figures, spin ordering is clearly discernible, even though the right panel contains a domain wall. A closer examination of the configuration for $J_2 = 0.3$ suggests that the order is a $3q$ order [36] (see Fig. 5).

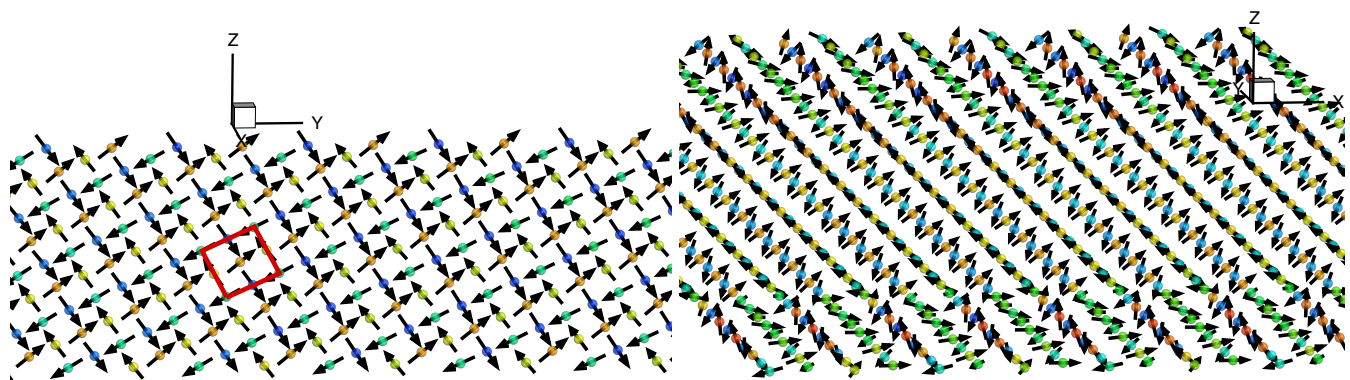


FIG. 4. Snapshots of the spin configuration in an M plane for $B = 0.4$, $K = 0.1$, $D = 0$, $J_3 = 0.2$, $J_2 = 0.3$ (left panel), $J_2 = 0.5$ (right panel), and $k_B T \approx 0.01$. The arrows show the three-dimensional (3D) spin orientation, and the color coding denotes the z component of the spins with the same color scale as in Fig. 3. For $J_2 = 0.3$, the spins depicted are almost in a single-domain $3q$ state (there is a domain wall toward the right end of the figure). In the right panel ($J_2 = 0.5$), several domains are visible. The largest domain in the center of the figure is not a $3q$ state, as a clear twist of the spins is visible along the y axis; this is probably a $2q$ state in which \mathbf{q}_2 is incommensurate with the lattice.

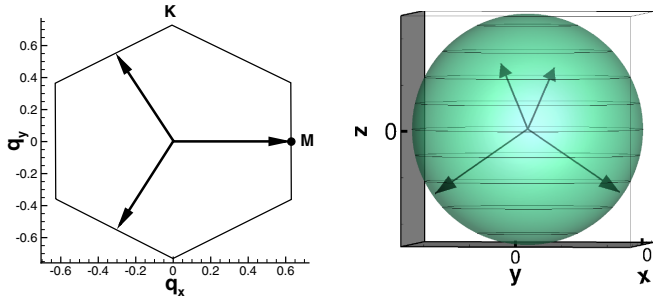


FIG. 5. The left panel shows a cartoon of the three wave vectors of the $3q$ state. The three vectors extend from the zone center to three M points on the Brillouin zone (BZ) boundary, 120° apart. The right panel shows a real-space depiction of the four spins in a magnetic unit cell. The four spins point toward four different corners in the spin-space unit cube, e.g., $(-1, 1, 1)$, $(1, -1, 1)$, $(-1, -1, -1)$, and $(1, 1, -1)$, such that the sum of the spins is zero.

Figure 6 shows a snapshot of the order in the ab plane for $B = 0.3$, $K = 0.1$, $D = 0$, $J_2 = 0.05$, $J_3 = 0.2$, and $k_B T \approx 0.01$. In this figure, the order is clearly the classic Néel order, which can be described as a $1q$ order with the wave vector q at a point K in the BZ. Figure 7 similarly shows snapshots for $J_2 = 0.25$ (left panel) and $J_2 = 0.35$ (right panel). At $J_2 = 0.25$, the system again exhibits the $3q$ state, while at $J_2 = 0.35$, the order has a short wavelength along the y direction, and a much longer wavelength is discernible along the x direction, visible as a gentle twist of the spins. The finite- T atomistic simulations thus confirmed the trivial OOP order, which allowed us to reduce the model to a 2D in-plane model. The 2D model is given by

$$\mathcal{H} = H_{\text{exchange}} + H_{\text{nnex}} + H_{\text{DMI}} + H_{\text{biq}} + H_{\text{ani}} + H_Z, \quad (13)$$

with lattice vectors which we write as

$$\begin{aligned} \mathbf{b}_1 &= \frac{\sqrt{3}}{2}a\hat{x} + \frac{a}{2}\hat{y} + 0\hat{z}, \\ \mathbf{b}_2 &= a\hat{y}, \\ \mathbf{b}_3 &= c\hat{z}, \end{aligned} \quad (14)$$

where \mathbf{b}_3 is irrelevant, and $a = 5.768 \text{ \AA}$. The reciprocal lattice vectors are then

$$\begin{aligned} \bar{\mathbf{b}}_1 &= \frac{\mathbf{b}_2 \cdot \mathbf{b}_3}{\mathbf{b}_1 \cdot (\mathbf{b}_2 \cdot \mathbf{b}_3)} = \frac{4\pi}{\sqrt{3}a}\hat{x}, \\ \bar{\mathbf{b}}_2 &= \frac{\mathbf{b}_3 \cdot \mathbf{b}_1}{\mathbf{b}_1 \cdot (\mathbf{b}_2 \cdot \mathbf{b}_3)} = \frac{4\pi}{\sqrt{3}a} \left[\frac{\sqrt{3}}{2}\hat{y} - \frac{1}{2}\hat{x} \right], \\ \bar{\mathbf{b}}_3 &= \frac{\mathbf{b}_1 \cdot \mathbf{b}_2}{\mathbf{b}_1 \cdot (\mathbf{b}_2 \cdot \mathbf{b}_3)} = \frac{2\pi}{c}\hat{z}. \end{aligned} \quad (15)$$

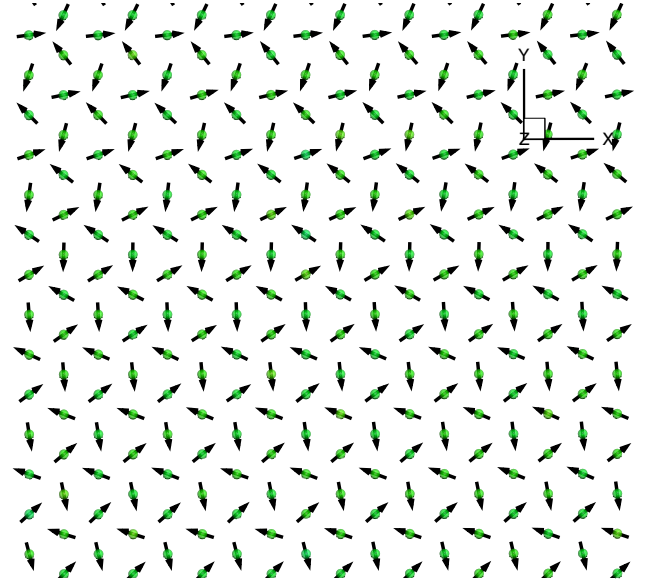


FIG. 6. Snapshot of the spin configuration in an M plane for $B = 0.3$, $K = 0.1$, $D = 0$, $J_2 = 0.05$, $J_3 = 0.2$, and $k_B T \approx 0.01$. The arrows show the three-dimensional (3D) spin orientation, and the color coding denotes the z component, which is here zero, of the spins with the same color scale as in Fig. 3. This state can readily be identified as a planar Néel state.

We will also use the vectors

$$\begin{aligned} \tau_1 &= \frac{\sqrt{3}}{2}a\hat{x} + \frac{a}{2}\hat{y} + 0\hat{z}, \\ \tau_2 &= -\frac{\sqrt{3}}{2}a\hat{x} + \frac{a}{2}\hat{y} + 0\hat{z}, \\ \tau_3 &= -a\hat{y}, \end{aligned} \quad (16)$$

that connect nearest-neighbor sites in an elementary triangular plaquette, with directions given by the DMI bonds in Fig. 2.

We will seek ground states among different classes of ordered states by constructing different *Ansätze* with variational parameters and minimizing the total energy with respect to those parameters. The variational states cover very general states with $1q$ and $2q$ orders and also include generalizations of the noncoplanar $3q$ state. While one can in general look for states the orders of which are characterized by multiple wave vectors using systematic Fourier expansions [3,8], such expansions can typically be terminated after two components as the weights of higher-order components decay exponentially and do not give rise to any physically meaningful effects [8]. We will therefore not construct higher-ordered states than the $1q$, $2q$, and $3q$ noncoplanar states as we believe these suffice to characterize the phase diagram of our model.

A $1q$ ordered state can be described by the *Ansatz*:

$$\mathbf{S}_{1q}(\mathbf{r}_i) = [A \cos(\mathbf{q} \cdot \mathbf{r}_i + \varphi), \sin(\mathbf{q} \cdot \mathbf{r}_i + \varphi), \sqrt{1 - A^2} \cos(\mathbf{q} \cdot \mathbf{r}_i + \varphi)], \quad (17)$$

where $-1 \leq A \leq 1$, φ is an arbitrary phase with $0 \leq \varphi \leq 2\pi$, and \mathbf{q} is any wave vector in the 2D BZ. This *Ansatz* obviously preserves normalization of the spin at each site. Note that there are two other possibilities:

$$\mathbf{S}(\mathbf{r}_i) = [A \cos(\mathbf{q} \cdot \mathbf{r}_i + \varphi), \sqrt{1 - A^2} \cos(\mathbf{q} \cdot \mathbf{r}_i + \varphi), \sin(\mathbf{q} \cdot \mathbf{r}_i + \varphi)], \quad (18)$$

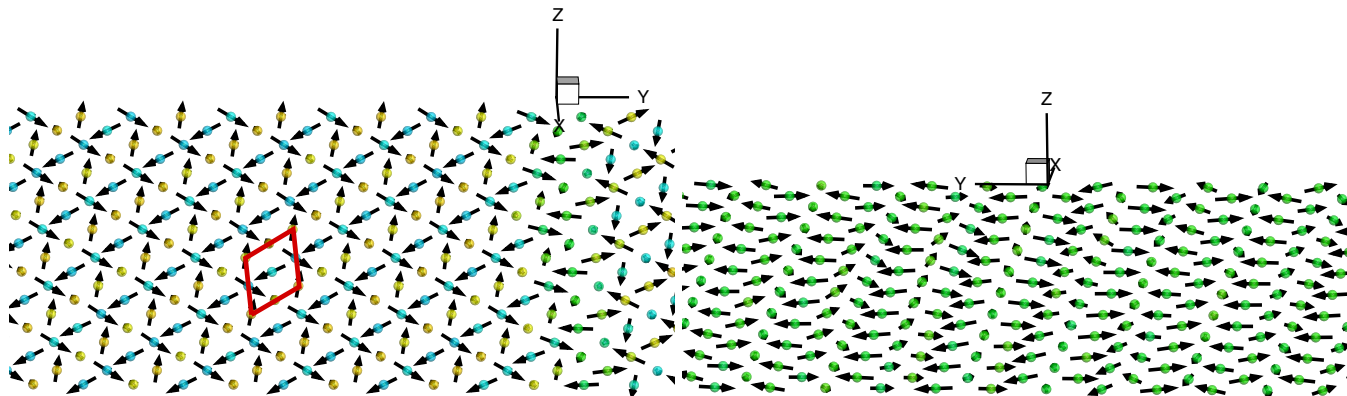


FIG. 7. Snapshots of the spin configuration in an M plane for $B = 0.3$, $K = 0.1$, $D = 0$, $J_3 = 0.2$, $J_2 = 0.25$ (left panel), $J_2 = 0.35$ (right panel), and $k_B T \approx 0.01$. The arrows show the three-dimensional (3D) spin orientation, and the color coding denotes the z component of the spins with the same color scale as in Fig. 3. For $J_2 = 0.25$ (left panel), the state can be identified as a $3q$ state, and a magnetic unit cell is indicated with red lines. For $J_2 = 0.35$ (right panel), the order is more complicated, and a gentle twist along the x axis can be observed.

and

$$\mathbf{S}(\mathbf{r}_i) = [\sin(\mathbf{q} \cdot \mathbf{r}_i + \varphi), A \cos(\mathbf{q} \cdot \mathbf{r}_i + \varphi), \sqrt{1 - A^2} \cos(\mathbf{q} \cdot \mathbf{r}_i + \varphi)]. \quad (19)$$

To further generalize the variational $1q$ spin states, we also perform a global $SO(3)$ rotation $\mathcal{R}(\theta_r, \mathbf{w})$ of all spins, where $\mathcal{R}(\theta_r, \mathbf{w})$ rotates the spin an angle θ_r about the unit vector \mathbf{w} : $\mathbf{S}(\mathbf{r}_i) \rightarrow \mathcal{R}(\theta_r, \mathbf{w})\mathbf{S}(\mathbf{r}_i)$. This yields seven variational parameters A , q_x , q_y , φ , θ_r , w_x , and w_y . Finally, in the presence of an external magnetic field along the z axis, we must allow for a small z component of the spins induced by the external field. We add this in the following way. We start with a given set of A , q_x , q_y , and φ and then perform the $SO(3)$ rotation for a given θ_r , w_x , and w_y of all spins. We then add a small z component $\delta z \ll 1$ to all spins. This breaks the normalization of the spins, so a final step is to renormalize all spins by dividing each spin by its norm. In numerical optimizations of the $1q$ and $2q$ states with an applied field, we ensure that the field is small enough that the resulting component δz is indeed smaller than 0.1.

Without an external magnetic field, we expect the three variational *Ansätze* Eqs. (17)–(19) to be degenerate in energy, at least for $D = 0$. This was indeed confirmed in the numerical minimization with respect to the variational parameters and served as a convenient check on the numerical minimizations.

We construct variational $2q$ states by a simple generalization of the *Ansätze* Eqs. (17)–(19) by replacing the constant amplitude A and $\sqrt{1 - A^2}$ for spin $\mathbf{S}(\mathbf{r}_i)$ by $\cos(\mathbf{q}_2 \cdot \mathbf{r}_i)$ and $\sin(\mathbf{q}_2 \cdot \mathbf{r}_i)$, respectively. Just as for the $1q$ variational states, we perform a global $SO(3)$ rotation for a given set of q_x , q_y , q_{x2} , q_{y2} , and φ . In the presence of an external magnetic field, we add a z component δz to all spins after the $SO(3)$ rotation and then renormalize the spins. Note that these variational $2q$ states include the $1q$ ones as special cases. This provided another check on the numerical minimizations. Figure 8 shows examples of an optimized $1q$ spin state for $B = 0.4$, $K = 0.1$,

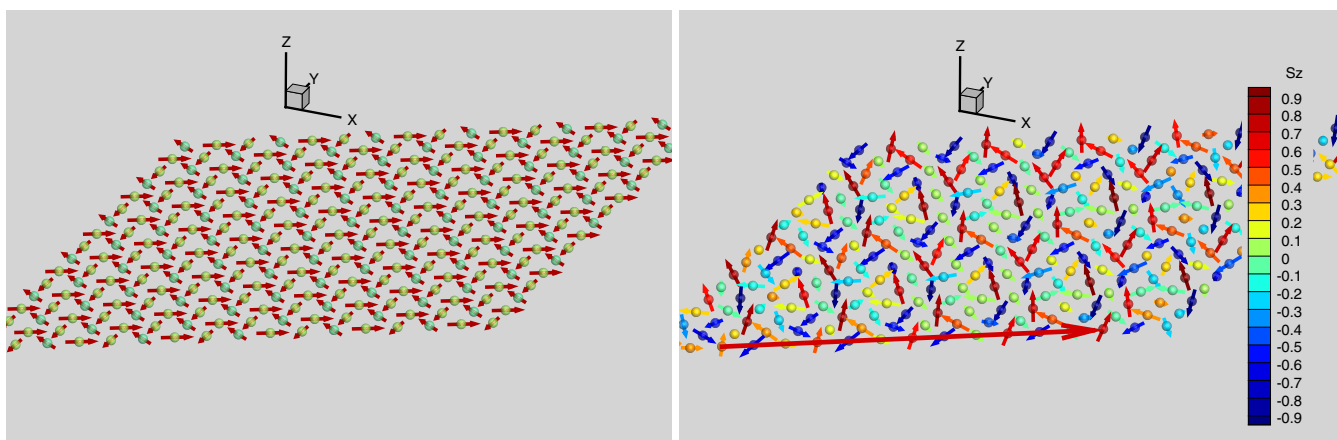


FIG. 8. $1q$ (left panel) and $2q$ (right panel) variational solutions for $B = 0.4$, $D = 0$, $J_2 = 0.04$ ($1q$), and $J_2 = 0.48$ ($2q$). The $1q$ state is a planar Néel state (the color coding of the arrows is in this case just for better visibility). In the right panel, a lattice direction along the a axis is indicated. The spins have an almost commensurate periodicity of period three along this direction.

$D = 0$, and $J_2 = 0.04$ and an optimized $2q$ spin state for $B = 0.4$, $K = 0.1$, $D = 0$, and $J_2 = 0.48$. The $1q$ spin state is planar. The $2q$ state is noncoplanar and has a rather complicated real-space texture, but certain features can be discerned. For example, along the a axis, as indicated in the figure, the spins have an almost commensurate period of three lattice spacings. It is not quite commensurate as the spins are twisted slightly away from each other at every third site.

For the 2D model with near-neighbor, next-nearest-neighbor, and biquadratic exchange and a small OOP anisotropy (e.g., $K \approx 0.05$ or $K \approx 0.1$), with the c axis a hard axis, there is a parameter range with J_2 smaller than unity where an in-plane so-called $3q$ state is the ground state [36], in which the spin state is given by

$$\mathbf{S}_{3q}(\mathbf{r}_i) = [\mathcal{S}_1 \cos(\mathbf{q}_1 \cdot \mathbf{r}_i), \mathcal{S}_2 \cos(\mathbf{q}_2 \cdot \mathbf{r}_i), \mathcal{S}_3 \cos(\mathbf{q}_3 \cdot \mathbf{r}_i)], \quad (20)$$

where \mathcal{S}_i are amplitudes with $\sum_{i=1}^3 \mathcal{S}_i^2 = 1$. The vectors \mathbf{q}_i extend from the Γ point in the BZ to three M points such that

$$\mathbf{S}(\mathbf{r}_i) = [\cos(\varphi_j) \sin(\theta_j) \cos(\mathbf{q}_1 \cdot \mathbf{r}_i), \sin(\varphi_j) \sin(\theta_j) \cos(\mathbf{q}_2 \cdot \mathbf{r}_i), \cos(\theta_j) \cos(\mathbf{q}_3 \cdot \mathbf{r}_i)], \quad (21)$$

where θ_j and φ_j , $j = 1, 2$ are additional variational parameters, and j enumerates the two sublattices with positive and negative \mathcal{S}_3 . This *Ansatz* with four variational parameters then also allows for an OOP net magnetization driven either by interactions or by an applied external field as the magnitude of the z component of the spin can be different on one sublattice from the other.

In the absence of DMI and for $K = 0$, the $3q$ state is degenerate under arbitrary $SO(3)$ rotations of all spins. In the presence of DMI and anisotropy, this is generally no longer the case. However, with the c axis a hard axis and with the DMI vector also along the c axis, the Hamiltonian is invariant under arbitrary global spin rotations about the c axis. There is then another readily identified spin state with net zero magnetization compatible with the lattice symmetry. This state also has four spins per unit cell, with one spin \mathbf{S}_0 along the z axis or perpendicular to the z axis and the other three with components equal to $\frac{1}{3}$ in magnitude with opposite sign to the z or in-plane component of \mathbf{S}_0 and with the components perpendicular to \mathbf{S}_0 120° apart (see Fig. 9 for a depiction with \mathbf{S}_0 along the $-z$ axis.) For the parameter range examined here, this state has higher energy than the $3q$ state, and we will ignore it from now on.

For a given set of input parameters J_2, D, B, K , and external field $H_z \hat{z}$, we then minimize the total energy per spin with respect to the parameters θ_j and φ_j for the $3q$ state and with respect to $A, q_x, q_y, \varphi, \theta_r, w_x, w_y$, and δz for the $1q$ and $2q$ spin spiral states. Because the interaction energy between nearest-neighbor spins only depends on their relative orientation, we can without loss of generality put one spin at the origin and calculate the interaction energy of this spin. For the $3q$ state, it suffices to calculate the total energy (interaction, anisotropy, and Zeeman) of the four inequivalent spins in the magnetic unit cell. For the $1q$ and $2q$ spin spiral states, however, we increase the sampling size: we first choose one central spin at the origin and calculate its interactions with its nearest neighbors and then add the interactions of the

the \mathbf{q} vectors are 120° apart (see Fig. 5). This yields a spin configuration with four inequivalent sites, so the magnetic unit cell has four sites (see Fig. 7). In the absence of a DMI, the magnetizations on the four sites are related by reflection or inversion, so there are only two degrees of freedom needed to specify the spin arrangement. These can be thought of as the magnitude of the spin projection on the z axis and a rotation about the z axis. For $B = 0$, the spin arrangement forms an a coplanar AFM with the amplitude of the z component $\mathcal{S}_3 = 0$. A small positive biquadratic coupling B (in our case already for $B = 0.025$) can drive \mathcal{S}_3 nonzero, yielding a noncoplanar AFM. A nonzero DMI or an applied external field can potentially break the symmetry relations between the spin orientations on the four different sites; the magnitude of the z component \mathcal{S}_3 can on the sites with $\mathcal{S}_3 < 0$ be different from the sites with $\mathcal{S}_3 > 0$. To allow for this possibility, we construct a bipartite model with positive and negative z components of the spin and seek solutions of the form:

six nearest-neighbor spins with their nearest neighbors for a total of 30 bonds. Because the $1q$ and $2q$ spin spiral states can have a long period, it is important to accurately include the anisotropy energy, as easy-plane anisotropy frustrates the DMI. The anisotropy energy and the Zeeman energy are therefore averaged over a large supercell with N_{site} sites, *i.e.*,

$$E_Z/\text{Spin} = -\frac{1}{N_{\text{sites}}} \mathbf{H}_{\text{ext}} \cdot \sum_{n_a, n_b} \mathbf{S}[\mathbf{q} \cdot (n_a \mathbf{b}_1 + n_b \mathbf{b}_2) + \varphi], \quad (22)$$

with N_{sites} typically 16×16 to 25×25 . We directly minimize the energy total energy per spin with respect to variational parameters of the $3q$ and spin spiral states to obtain the variational ground state.

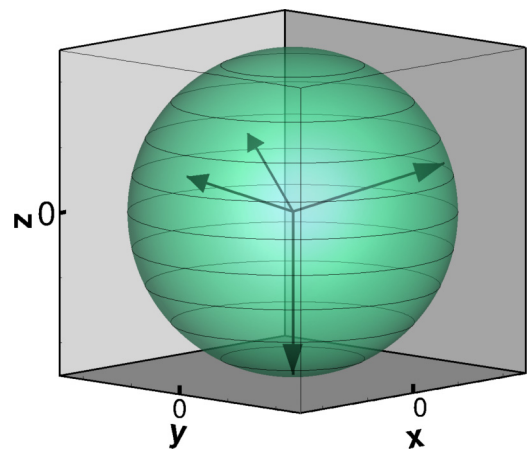


FIG. 9. Depiction of another class of spin states with the four spins from one magnetic unit cell inserted in the unit cube in spin space. One spin has positive or negative z component (here shown with negative z component), and the others have z components of opposite sign and the spin components in the xy plane 120° apart.

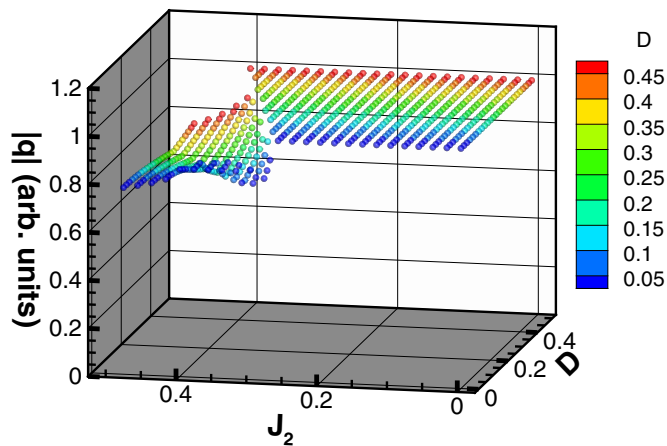


FIG. 10. The evolution of the norm of \mathbf{q} normalized to the K point in the Brillouin zone (BZ) for the $1q$ state as a function of J_2 and D for $B = 0.3$ and $K = 0.1$. The color coding indicates the value of D . $|\mathbf{q}|$ is unity, as \mathbf{q} is at a K point for small J_2 and D . For J_2 above some critical value, the norm of \mathbf{q} starts to decrease as \mathbf{q} moves from the K points in toward the zone center Γ . This critical value of J_2 increases slightly with D .

As discussed earlier, a collinear AFM cannot yield a nonzero AHE, and a coplanar AFM has no contribution to the AHE from the spin chirality. The AHE is directly related to the chirality χ of the spin structure which we calculate as

$$\chi = \epsilon_{ijk} \mathbf{S}(\tau_i) \cdot [\mathbf{S}(\tau_j) \cdot \mathbf{S}(\tau_k)], \quad (23)$$

where $\epsilon_{\alpha\beta\gamma}$ is the Levi-Civita symbol, repeated indices are summed over, and the sites i , j , and k form an elementary triangular plaquette.

We explored the phase space for a range of B between 0.025 and 0.4, and K ranging from 0.025 to 0.1. The resulting

phase diagram evolves slowly with varying B and K ; the dependence on K is rather weak. We will therefore typically discuss results for B in the range of 0.3 to 0.4, with $K = 0.05$ or 0.1.

III. RESULTS AND DISCUSSION

For zero DMI coupling D , zero next-nearest-neighbor coupling J_2 , and for all values of B we have examined, the ground state is the well-known Néel triangular AFM state with the three spins on an elementary triangular plaquette 120° apart, and with the OOP anisotropy $K > 0$, the spins are coplanar in the xy plane (see Fig. 8). This state is captured by the $1q$ and $2q$ *Ansätze* but not by the $3q$ *Ansatz*, and the $1q$ and $2q$ states correctly yield the ground state. Because the spins are coplanar, the state has a vanishing chirality and therefore vanishing anomalous Hall conductivity. When the interactions B , J_2 , and D are increasing from zero, the spin structure becomes more complicated. For small J_2 in the range of 0.1 at $D = 0$ to ~ 0.3 at $D = 0.5$, the $1q$ state is always lower in energy than the $2q$ state (the $2q$ variational state collapses to the $1q$ state; we also confirmed numerically that the $1q$ and $2q$ *Ansätze* are degenerate for small J_2).

Figure 10 shows $|\mathbf{q}|$ normalized to the K point in the first BZ in the $1q$ state as function of J_2 and D for $B = 0.3$ and $K = 0.1$. For small J_2 and D , \mathbf{q} falls on the K points, and the state is a planar Néel state. As J_2 increases above some critical value that depends weakly on D , \mathbf{q} moves in toward the zone center Γ as the interaction parameters try to drive the system toward an incommensurate spiral that is in general nonplanar. If B is too small, $B \lesssim 0.3$ (a value that depends very weakly on K), the interactions cannot drive \mathbf{q} away from the BZ boundary, and instead of moving in toward Γ , \mathbf{q} moves on the BZ boundary. For the $2q$ state, \mathbf{q} in general falls on the K points on the BZ boundary (see Fig. 11). For small J_2 ,

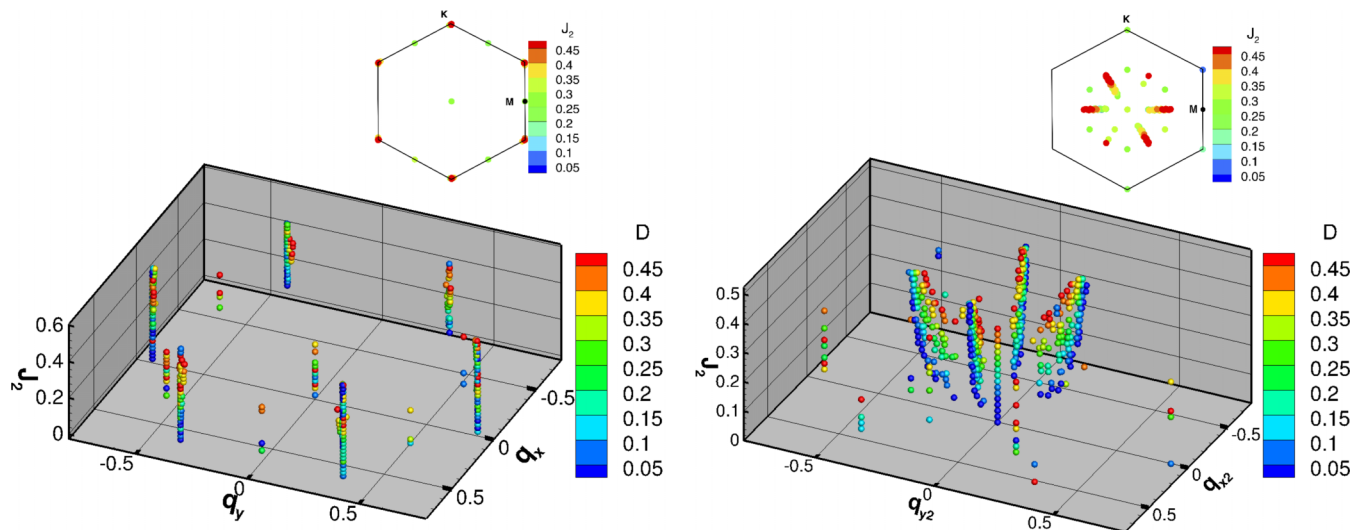


FIG. 11. The panels show the evolution of wave vectors \mathbf{q} (left panel) and \mathbf{q}_2 (right panel) for the $2q$ state as function of J_2 for $B = 0.3$ and $K = 0.1$. The color coding indicates the value of D . The insets show the positions of the wave vectors in the 1st Brillouin zone (BZ), with the color coding denoting J_2 . \mathbf{q} is generally at the K -points but move slightly inwards towards the zone center as D increases, more so as B decreases below $B = 0.3$. Occasionally for small values of J_2 , $J_2 \lesssim 0.2$, \mathbf{q} is at the Γ or at M points, in which case \mathbf{q}_2 is at the K points or halfway to the K points. \mathbf{q}_2 moves towards the M points from Γ approximately as the square root of J_2 with increasing J_2 ; as D increases, a larger J_2 is required to move \mathbf{q}_2 from the zone center.

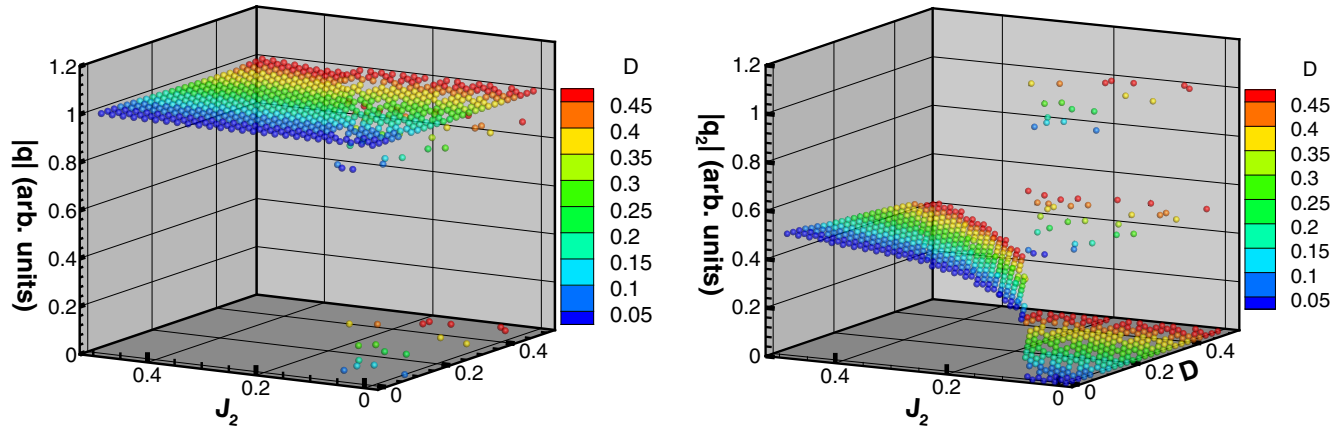


FIG. 12. The evolution of $|\mathbf{q}|$ (left panel) and $|\mathbf{q}_2|$ (right panel) normalized to the K point in the Brillouin zone (BZ) for the $2q$ state as a function of J_2 and D for $B = 0.3$ and $K = 0.1$. The color coding indicates the value of D . $|\mathbf{q}|$ is unity, as \mathbf{q} is at a K point for small J_2 and D , except for a few scattered points; these are all just other representations of the $1q$ state. $|\mathbf{q}_2|$ is zero for small J_2 and D but starts to grow as J_2 exceeds a critical value that depends on D and grows approximately linearly with D : when $D = 0$, this critical value is ~ 0.06 , and when $D = 0.5$, the critical value is ~ 0.3 . The critical value $J_2(D)$ marks the transition from a $1q$ ground state to a $2q$ ground state.

$J_2 \lesssim 0.1$, \mathbf{q}_2 is at the zone center Γ (which makes the state a $1q$ state) but increases approximately as the square root of J_2 with increasing J_2 and moves toward the M points, stopping halfway to the M points; the larger D is, the larger J_2 has to be for \mathbf{q}_2 to start moving from the zone center. For a few values of J_2 and D , generally with $J_2 \lesssim 0.2$, \mathbf{q} falls at the M points and \mathbf{q}_2 on the K points; these particular $2q$ states are in fact another representation of $1q$ states. Figure 11 also displays a sixfold symmetry, as we have not folded the obtained values of \mathbf{q} and \mathbf{q}_2 back to an irreducible wedge of the 2S BZ. Figure 12 shows the evolution of $|\mathbf{q}|$ and $|\mathbf{q}_2|$ normalized to the K point in the $2q$ state as functions of J_2 and D . For small J_2 and D , \mathbf{q} is on a K point and $\mathbf{q}_2 = 0$, and the $2q$ state is equivalent to the $1q$ (this is also the case for the few scattered points at which \mathbf{q} is at M points or is zero). For some critical value of J_2 , the norm of \mathbf{q}_2 suddenly increases, and \mathbf{q}_2 starts to move toward M points in the BZ with $|\mathbf{q}_2|$ growing approximately as $\sqrt{J_2}$. The critical value of J_2 depends on D and is ~ 0.06 for $D = 0$ and ~ 0.3 for $D = 0.5$; this critical value is the transition from a $1q$ ground state to a $2q$ ground state. The critical value is almost independent of B and very weakly dependent on K . The noncoplanar $3q$ state is stabilized for $B > 0$ by $J_2 > 0$. The dependence on B is stronger than for the spin spiral states, in that the magnitude of the z component of the spins S_z and the chirality increase rapidly with B for fixed K (see Fig. 13). The dependence on K is weak, except that for very small B , $B \lesssim 0.025$, the chirality and S_z components are zero for K too large, $K \gtrsim 0.05$. In contrast, the chirality of the $1q$ spin spiral state is always zero. The net magnetization is zero in the absence of an external field. The energy of the $3q$ state is also independent of D .

While the $1q$ (or $2q$) state yields the correct ground state for $B = D = J_2 = 0$, for small but finite B and J_2 , we would expect the ground state of CoNb_3S_6 to be the $3q$ state based on electronic structure calculations [49]; these also confirm that this state has a nonzero AHE. This implies that there must be a transition from a spin spiral to a $3q$ state as the interaction parameters are increased. This, in turn, makes it interesting to explore the phase diagram of this system as a

transition between $3q$ and spin spiral states could have an immediate observable consequence in the AHE. Figure 14 depicts the energy surfaces of the $2q$ and $3q$ states for $B = 0.4$ and $K = 0.1$. While the energy for the $3q$ state is independent of D and decreases linearly with increasing J_2 , the energy surface of the $2q$ state has a local maximum as a function of J_2 for fixed D . As a consequence, the two energy surfaces intersect at large enough B , $B \gtrsim 0.3$, for small D , and the $3q$ state has lower energy for a range of D and J_2 .

Figure 15 shows the phase diagrams in the D - J_2 space for $K = 0.1$ with $B = 0.3$ and 0.4 . The $3q$ state occupies a region with small D and nonzero J_2 . For $B = 0.3$, this phase is barely visible near $D = 0$. As B increases, this region increases in size. For $B = 0.4$, the $3q$ state occupies a small strip near $D = 0$ for small $J_2 \lesssim 0.1$. The $1q$ state is always the ground state for small J_2 . The phase diagram does not change much as B

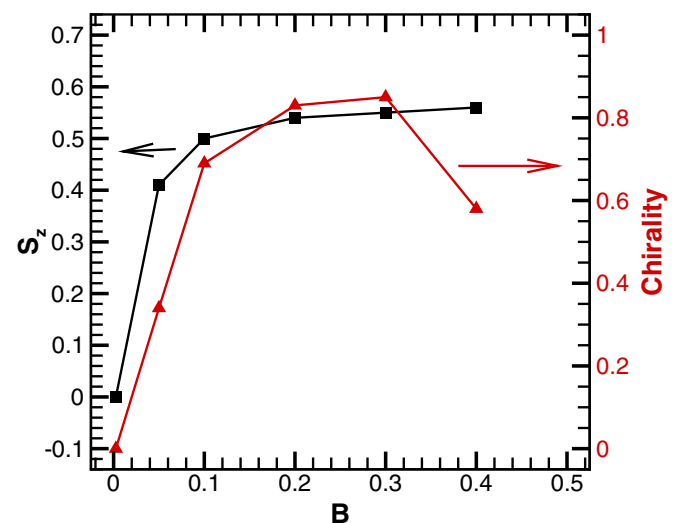


FIG. 13. Magnitude of the z components of the spins (black squares and black line) and average chirality (red diamonds and red line) in the $3q$ state as a function of B for $K = 0.1$ and $J_2 = 0$.

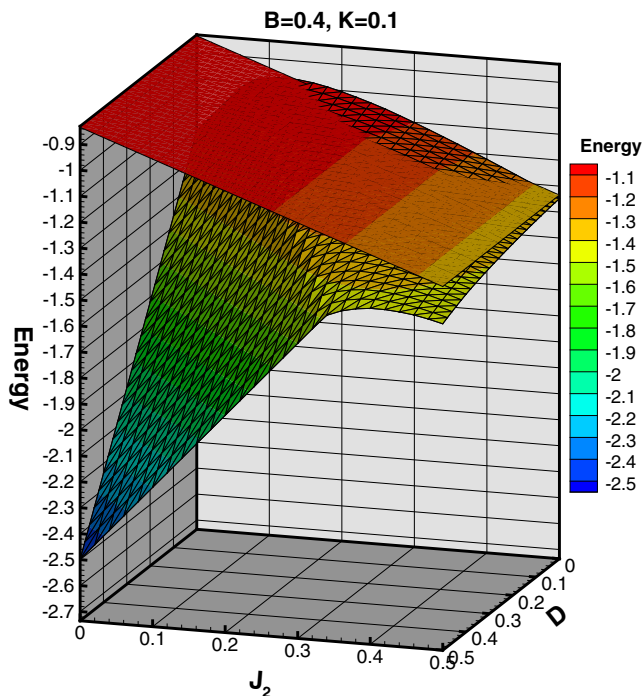


FIG. 14. Energy surfaces of the $2q$ state (hatched) and the $3q$ state for $B = 0.4$ and $K = 0.1$. The $3q$ state has lower energy as J_2 increases.

increases from 0.4 to 0.5. Furthermore, the dependence on K is weak; decreasing K by a factor of two from $K = 0.1$ to 0.05 only very slightly increases the region of the $3q$ state to larger D and a larger range of J_2 by <0.04 for J_2 and ~ 0.02 for D .

The transition from a coplanar Néel state to a noncoplanar $3q$ state with increasing J_2 and then to what appears to be a $2q$ state was also confirmed by finite- T 3D atomistic simulations

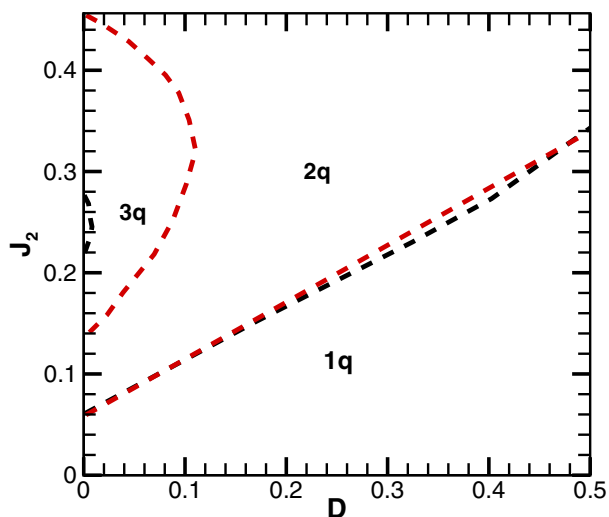


FIG. 15. Phase diagram on the D - J_2 space for $K = 0.1$ and for $B = 0.3$ (black dashed lines) and $B = 0.4$ (red lines). The $1q$ state occupies the phase diagram for small J_2 . The $3q$ phase emerges near $D = 0$ for $J_2 \sim 0.25$ as B increases.

using the s-LLG equation [51], as detailed earlier in this section.

The $1q$ state has zero chirality because of symmetry and is also a planar state with the magnetization in the ab plane in the parameter space that we have examined here; as stated earlier, the $3q$ state has a nonzero chirality. For the optimized $3q$ state, the chirality (averaged over a unit cell) depends strongly on B for small B (see Fig. 13) but very weakly on the other parameters. The $2q$ state has different chirality properties. The local chirality evaluated over any elementary plaquette is in general nonzero as the spins are in general coplanar. However, the chirality oscillates in magnitude and changes sign in space from one triangular plaquette to the next, and the chirality is zero when averaged over several plaquettes. This implies that the AHE arising from spin chirality is zero in the $2q$ state as well as in the $1q$ state with its zero chirality. Therefore, the $1q$ and $2q$ spin spiral states cannot give rise to a Berry phase and a nonzero AHE from the spin chirality alone, while the $3q$ state can.

The $1q$, $2q$, and $3q$ states all have net zero magnetization along any axis. The OOP susceptibility for the $1q$, $2q$, and $3q$ states is small and relatively uninteresting, at least for the parameter ranges we have investigated. For fields up to $H_z = 0.1$, the average S_z component $\langle S_z \rangle$ grows linearly by a small amount of up to ~ 0.01 . A small OOP susceptibility is consistent with the results for CoNb_3S_6 by Ghimire *et al.* [44].

IV. CONCLUSIONS AND SUMMARY

We have here proposed and analyzed a model for the in-plane magnetic interactions in the family of triangular AFMs in transition-metal intercalated dichalcogenides $(M)\text{Nb}_3\text{S}_6$. The model allows us to search for three general classes of magnetic ground states: $1q$ and $2q$ spin spiral states and a $3q$ state with four spins per unit cell. For small in-plane next-nearest-neighbor interactions $J_2 \lesssim 0.1$, the $1q$ spin spiral state is the ground state, but with increasing J_2 , the system transitions to a $2q$ state which generally is noncoplanar. A nonzero J_2 leads to a $3q$ ground state stabilized by a nonzero B . For $B \gtrsim 0.3$, the noncoplanar $3q$ state emerges as the ground state for a range of the DMI $D \geq 0$. The $1q$ and $2q$ states have vanishing chirality $\chi = \mathbf{S}_1 \cdot (\mathbf{S}_2 \times \mathbf{S}_3)$ evaluated over the three spins in an elementary triangular plaquette and averaged over many plaquettes, and so the spin chirality will not contribute to an AHE signal for these states. The noncoplanar $3q$ state has a nonzero chirality. In a 3D system, this gives rise to a nonzero AHE provided the stacked 2D layers have the same chirality; a large nonzero AHE is consistent with measurements [44,48] on CoNb_3S_6 and electronic structure calculations that include spin-orbit interactions [49]. While our model suggests that the $3q$ structure in CoNb_3S_6 can give rise to an observed AHE, we cannot make any quantitative predictions about the magnitude of the quantum Hall conductivity. This is because CoNb_3S_6 is a metal with the Co-hybridized bands crossing the Fermi level [49]. Therefore, the actual values of the anomalous Hall conductivity depend sensitively on the details of the electronic structure and are beyond the scope of this paper. However, increasing D drives the system to nonchiral $2q$ or $1q$ states, as the DMI with its vector along the c axis favors planar spins. Furthermore, too

small B cannot stabilize the $3q$ state. Therefore, the observed AHE [44,48] puts constraints on D and B : B must be $\sim >0.2$, and D must be $<\sim 0.1$ to drive the system to a $3q$ with nonzero chirality.

The sensitivity of the ground state to interaction parameters opens the intriguing possibility of inducing a transition between the $3q$ state and the spin spiral states by, for example, biaxial in-plane strain. Another potential mechanism is substitutional doping, e.g., Mn for Co. The MnNb_3S_6 ground state is a planar FM [49], presumably because of stronger double exchange, and Mn is much more likely to occupy Co sites than interstitial or Nb/S sites. Doping may change the magnetic interactions (and also the electron filling) and induce a transition, although there is a small possibility that doping may lead to more complicated interactions not considered here. Such a transition from $3q$ to $2q$ or $1q$ states induced by strain or

doping should have a clear signature in the magnetotransport properties.

ACKNOWLEDGMENTS

We gratefully acknowledge insightful conversations with I. Martin and J. F. Mitchell. O.H. and H.P. acknowledge funding from the U.S. Department of Energy, Office of Science, Basic Energy Sciences Division of Materials Sciences and Engineering. R.A.H. received funding from the European Research Council under the European Union's Horizon 2020 research and innovation programme (Grant Agreement No. 882340). We gratefully acknowledge the computing resources provided on Bebop, Swing, and Blues high-performance computing clusters operated by the Laboratory Computing Resource Center at Argonne National Laboratory.

-
- [1] S. Mühlbauer, B. Binz, F. Jonietz, C. Pfleiderer, A. Rosch, A. Neubauer, R. Georgii, and P. Böni, Skyrmion lattice in a chiral magnet, *Science* **323**, 915 (2009).
- [2] N. Nagaosa, J. Sinova, S. Onoda, A. H. MacDonald, and N. P. Ong, Anomalous Hall effect, *Rev. Mod. Phys.* **82**, 1539 (2010).
- [3] A. Leonov and M. Mostovoy, Multiply periodic states and isolated skyrmions in an anisotropic frustrated magnet, *Nat. Commun.* **6**, 8275 (2015).
- [4] S. S.-L. Zhang, C. Phatak, A. Petford-Long, and O. Heinonen, Tailoring magnetic skyrmions by geometric confinement of magnetic structures, *Appl. Phys. Lett.* **111**, 242405 (2017).
- [5] R. Moessner and J. T. Chalker, Low-temperature properties of classical geometrically frustrated antiferromagnets, *Phys. Rev. B* **58**, 12049 (1998).
- [6] G. H. Wannier, Antiferromagnetism. The triangular Ising net, *Phys. Rev.* **79**, 357 (1950).
- [7] M. Collins and O. Petrenko, Review/synthèse: Triangular antiferromagnets, *Can. J. Phys.* **75**, 605 (1997).
- [8] C. Liu, R. Yu, and X. Wang, Semiclassical ground-state phase diagram and multi- Q phase of a spin-orbit-coupled model on triangular lattice, *Phys. Rev. B* **94**, 174424 (2016).
- [9] J. N. Reimers and A. J. Berlinsky, Order by disorder in the classical Heisenberg kagomé antiferromagnet, *Phys. Rev. B* **48**, 9539 (1993).
- [10] M. E. Zhitomirsky, Octupolar ordering of classical kagome antiferromagnets in two and three dimensions, *Phys. Rev. B* **78**, 094423 (2008).
- [11] M. Gvozdikova, P. Melchy, and M. Zhitomirsky, Magnetic phase diagrams of classical triangular and kagome antiferromagnets, *J. Phys.: Condens. Matter* **23**, 164209 (2011).
- [12] V. Grison, P. Viot, B. Bernu, and L. Messio, Emergent Potts order in the kagome $J_1 - J_3$ Heisenberg model, *Phys. Rev. B* **102**, 214424 (2020).
- [13] H. Chen, Q. Niu, and A. H. MacDonald, Anomalous Hall Effect Arising from Noncollinear Antiferromagnetism, *Phys. Rev. Lett.* **112**, 017205 (2014).
- [14] S. Nakatsuji, N. Kiyohara, and T. Higo, Large anomalous Hall effect in a non-collinear antiferromagnet at room temperature, *Nature (London)* **527**, 212 (2015).
- [15] A. K. Nayak, J. E. Fischer, Y. Sun, B. Yan, J. Karel, A. C. Komarek, C. Shekhar, N. Kumar, W. Schnelle, J. Kübler *et al.*, Large anomalous Hall effect driven by a nonvanishing Berry curvature in the noncollinear antiferromagnet Mn_3Ge , *Sci. Adv.* **2**, e1501870 (2016).
- [16] Y. Zhang, Y. Sun, H. Yang, J. Železný, S. P. P. Parkin, C. Felser, and B. Yan, Strong anisotropic anomalous Hall effect and spin Hall effect in the chiral antiferromagnetic compounds Mn_3X ($X = \text{Ge}, \text{Sn}, \text{Ga}, \text{Ir}, \text{Rh}, \text{and Pt}$), *Phys. Rev. B* **95**, 075128 (2017).
- [17] M. Ikhlas, T. Tomita, T. Koretsune, M.-T. Suzuki, D. Nishio-Hamane, R. Arita, Y. Otani, and S. Nakatsuji, Large anomalous Nernst effect at room temperature in a chiral antiferromagnet, *Nat. Phys.* **13**, 1085 (2017).
- [18] T. Higo, H. Man, D. B. Gopman, L. Wu, T. Koretsune, O. M. van't Erve, Y. P. Kabanov, D. Rees, Y. Li, M.-T. Suzuki *et al.*, Large magneto-optical Kerr effect and imaging of magnetic octupole domains in an antiferromagnetic metal, *Nat. Photonics* **12**, 73 (2018).
- [19] M. Kimata, H. Chen, K. Kondou, S. Sugimoto, P. K. Muduli, M. Ikhlas, Y. Omori, T. Tomita, A. H. MacDonald, S. Nakatsuji *et al.*, Magnetic and magnetic inverse spin Hall effects in a non-collinear antiferromagnet, *Nature (London)* **565**, 627 (2019).
- [20] Y. Chen, J. Gaudet, S. Dasgupta, G. G. Marcus, J. Lin, T. Chen, T. Tomita, M. Ikhlas, Y. Zhao, W. C. Chen *et al.*, Antichiral spin order, its soft modes, and their hybridization with phonons in the topological semimetal Mn_3Ge , *Phys. Rev. B* **102**, 054403 (2020).
- [21] J.-X. Yin, W. Ma, T. A. Cochran, X. Xu, S. S. Zhang, H.-J. Tien, N. Shumiya, G. Cheng, K. Jiang, B. Lian *et al.*, Quantum-limit Chern topological magnetism in TbMn_6Sn_6 , *Nature (London)* **583**, 533 (2020).
- [22] N. J. Ghimire, R. L. Dally, L. Poudel, D. Jones, D. Michel, N. T. Magar, M. Bleuel, M. A. McGuire, J. Jiang, J. Mitchell *et al.*, Competing magnetic phases and fluctuation-driven scalar spin chirality in the kagome metal YMn_6Sn_6 , *Sci. Adv.* **6**, eabe2680 (2020).
- [23] T. Asaba, S. M. Thomas, M. Curtis, J. D. Thompson, E. D. Bauer, and F. Ronning, Anomalous Hall effect in the kagome ferrimagnet GdMn_6Sn_6 , *Phys. Rev. B* **101**, 174415 (2020).
- [24] W. Ma, X. Xu, J.-X. Yin, H. Yang, H. Zhou, Z.-J. Cheng, Y. Huang, Z. Qu, F. Wang, M. Z. Hasan *et al.*, Rare Earth Engineering in RMn_6Sn_6 ($R = \text{Gd-Tm}, \text{Lu}$) Topological Kagome Magnets, *Phys. Rev. Lett.* **126**, 246602 (2021).

- [25] S. Ereameev, M. Otrokov, and E. V. Chulkov, Competing rhombohedral and monoclinic crystal structures in MnPn_2Ch_4 compounds: An *ab-initio* study, *J. Alloys Compd.* **709**, 172 (2017).
- [26] M. M. Otrokov, T. V. Menshchikova, M. G. Vergniory, I. P. Rusinov, A. Y. Vyazovskaya, Y. M. Koroteev, G. Bihlmayer, A. Ernst, P. M. Echenique, A. Arnau *et al.*, Highly-ordered wide bandgap materials for quantized anomalous Hall and magnetoelectric effects, *2D Mater.* **4**, 025082 (2017).
- [27] M. M. Otrokov, I. I. Klimovskikh, H. Bentmann, D. Estyunin, A. Zeugner, Z. S. Aliev, S. Gaß, A. Wolter, A. Koroleva, A. M. Shikin *et al.*, Prediction and observation of an antiferromagnetic topological insulator, *Nature (London)* **576**, 416 (2019).
- [28] J. Li, Y. Li, S. Du, Z. Wang, B.-L. Gu, S.-C. Zhang, K. He, W. Duan, and Y. Xu, Intrinsic magnetic topological insulators in van der Waals layered MnBi_2Te_4 -family materials, *Sci. Adv.* **5**, eaaw5685 (2019).
- [29] Y. Deng, Y. Yu, M. Z. Shi, Z. Guo, Z. Xu, J. Wang, X. H. Chen, and Y. Zhang, Quantum anomalous Hall effect in intrinsic magnetic topological insulator MnBi_2Te_4 , *Science* **367**, 895 (2020).
- [30] M.-C. Chang and Q. Niu, Berry Phase, Hyperorbits, and the Hofstadter Spectrum, *Phys. Rev. Lett.* **75**, 1348 (1995).
- [31] M.-C. Chang and Q. Niu, Berry phase, hyperorbits, and the Hofstadter spectrum: semiclassical dynamics in magnetic Bloch bands, *Phys. Rev. B* **53**, 7010 (1996).
- [32] G. Sundaram and Q. Niu, Wave-packet dynamics in slowly perturbed crystals: Gradient corrections and Berry-phase effects, *Phys. Rev. B* **59**, 14915 (1999).
- [33] T. Jungwirth, Q. Niu, and A. H. MacDonald, Anomalous Hall Effect in Ferromagnetic Semiconductors, *Phys. Rev. Lett.* **88**, 207208 (2002).
- [34] D. Xiao, M.-C. Chang, and Q. Niu, Berry phase effects on electronic properties, *Rev. Mod. Phys.* **82**, 1959 (2010).
- [35] Y. Taguchi, Y. Oohara, H. Yoshizawa, N. Nagaosa, and Y. Tokura, Spin chirality, Berry phase, and anomalous Hall effect in a frustrated ferromagnet, *Science* **291**, 2573 (2001).
- [36] I. Martin and C. D. Batista, Itinerant Electron-Driven Chiral Magnetic Ordering and Spontaneous Quantum Hall Effect in Triangular Lattice Models, *Phys. Rev. Lett.* **101**, 156402 (2008).
- [37] S.-S. Zhang, H. Ishizuka, H. Zhang, G. B. Halász, and C. D. Batista, Real-space Berry curvature of itinerant electron systems with spin-orbit interaction, *Phys. Rev. B* **101**, 024420 (2020).
- [38] Y. Machida, S. Nakatsuji, S. Onoda, T. Tayama, and T. Sakakibara, Time-reversal symmetry breaking and spontaneous Hall effect without magnetic dipole order, *Nature (London)* **463**, 210 (2010).
- [39] Y. Kato, I. Martin, and C. D. Batista, Stability of Spontaneous Quantum Hall State in the Triangular Kondo-lattice Model, *Phys. Rev. Lett.* **105**, 266405 (2010).
- [40] D. Solenov, D. Mozyrsky, and I. Martin, Chirality Waves in Two-Dimensional Magnets, *Phys. Rev. Lett.* **108**, 096403 (2012).
- [41] A. Neubauer, C. Pfleiderer, B. Binz, A. Rosch, R. Ritz, P. G. Niklowitz, and P. Böni, Topological Hall Effect in the A Phase of MnSi , *Phys. Rev. Lett.* **102**, 186602 (2009).
- [42] R. Shindou and N. Nagaosa, Orbital Ferromagnetism and Anomalous Hall Effect in Antiferromagnets on the Distorted fcc Lattice, *Phys. Rev. Lett.* **87**, 116801 (2001).
- [43] C. Sürgers, G. Fischer, P. Winkel, and H. v. Löhneysen, Large topological Hall effect in the non-collinear phase of an antiferromagnet, *Nat. Commun.* **5**, 3400 (2014).
- [44] N. J. Ghimire, A. Botana, J. Jiang, J. Zhang, Y.-S. Chen, and J. Mitchell, Large anomalous Hall effect in the chiral-lattice antiferromagnet CoNb_3S_6 , *Nat. Commun.* **9**, 3280 (2018).
- [45] H. Takatsu, S. Yonezawa, S. Fujimoto, and Y. Maeno, Unconventional Anomalous Hall Effect in the Metallic Triangular-Lattice Magnet PdCrO_2 , *Phys. Rev. Lett.* **105**, 137201 (2010).
- [46] K. Anzenhofer, J. van den Berg, P. Cossee, and J. Helle, The crystal structure and magnetic susceptibilities of MnNb_3S_6 , FeNb_3S_6 , CoNb_3S_6 , and NiNb_3S_6 , *J. Phys. Chem. Solids* **31**, 1057 (1970).
- [47] S. Parkin, E. Marseglia, and P. Brown, Magnetic structure of $\text{Co}_{1/3}\text{NbS}_2$ and $\text{Co}_{1/3}\text{TaS}_2$, *J. Phys. C* **16**, 2765 (1983).
- [48] G. Tenasini, E. Martino, N. Ubrig, N. J. Ghimire, H. Berger, O. Zaharko, F. Wu, J. F. Mitchell, I. Martin, L. Forró, and A. F. Morpurgo, Giant anomalous Hall effect in quasi-two-dimensional layered antiferromagnet $\text{Co}_{1/3}\text{NbS}_2$, *Phys. Rev. Research* **2**, 023051 (2020).
- [49] H. Park, O. Heinonen, and I. Martin, First-principles study of magnetic states and the anomalous Hall conductivity of MNb_3S_6 ($M = \text{Co}, \text{Fe}, \text{Mn}, \text{and Ni}$), *arXiv:2110.03029* [cond-mat.mtrl-sci].
- [50] J. Reimers and J. Dahn, Lattice gas and spin ordering on stacked triangular lattices, *J. Phys.: Condens. Matter* **4**, 8105 (1992).
- [51] J. L. García-Palacios and F. J. Lázaro, Langevin-dynamics study of the dynamical properties of small magnetic particles, *Phys. Rev. B* **58**, 14937 (1998).
- [52] R. F. L. Evans, W. J. Fan, P. Chureemart, T. A. Ostler, M. O. A. Ellis, and R. W. Chantrell, Atomistic Spin Model Simulations of Magnetic Nanomaterials, *J. Phys.: Condens. Matter* **26**, 103202 (2014).